Geophysical Research Letters

Supporting Information for

Identifying sensitive ranges in global warming precipitation change dependence on convective parameters.

Diana N. Bernstein[1,2] and J. David Neelin[1]

[1]Department of Atmospheric and Oceanic Sciences, University of California Los Angeles, Los Angeles, CA, 90095, USA

[2]Department of Soil and Water Sciences, Robert H. Smith Faculty of Agriculture, Food and Environment, The Hebrew University of Jerusalem, POB 12, Rehovot 76100, Israel

Contents of this file

Introduction

Text S1 and the accompanying figures S1-S3 provide additional details supporting the main text:

- details on simulation set up;
- a demonstration of rapid equilibration as a function of simulation time of a key hydrological cycle measure, showing the case of sensitivity to entrainment across the full feasible range as the case with the largest changes (Text S1 and Fig. S1);
- details on the error bar computations in main text figures Fig. 1 and Fig. 3;
- the December-February precipitation change and precipitation change sensitivities corresponding to Figure. 2 of the main text (Text S1 and Fig. S2);
- examples of CMIP5 archive precipitation change similar to Fig 2a of the main text for reference (Fig. S3).

Text S1.

In this study, simulations of precipitation change under the global warming Representative Concentration Pathway (RCP) 8.5 scenario, use a branch-run methodology to minimize spin-up (in CESM technical terms these are hybrid runs with ocean and sea ice using a restart file and atmosphere/land initialized). Runs with different parameter settings are restarted from the year 1976 for the historical period and from 2071 for the end-of-century simulation under RCP 8.5 scenario using a restart files from the standard parameter simulation with the Community Climate System Model 4 (CCSM4; i.e., a subset of CESM1). This CCSM4 "restart run" is used only to provide initial conditions; it likewise followed the CMIP5 historical forcing and RCP8.5 scenario protocol. The standard parameter CESM1 control is created from an ensemble of runs using this methodology to have a precise comparison to the parameter perturbation runs in CESM1. A control ensemble of 15 runs with standard parameter values (CESM1 default values), is created from a set of branch ensemble members each restarted with initial conditions changed to values from a different year (January 1, 1970-1984 and 2066-2077) in the control run to yield different evolutions of the internal variability. The year for the analysis is set by the radiative forcing as a function of time which begins in each case from the same year, 1976 and 2071 respectively. For each of the periods, historical and end-of-century, a 30-year run is performed (1976-2005 and 2071-2100, respectively), and only last 20 years are used for the analysis, allowing 10 years for equilibration.

Equilibration.

Figure S1 shows an example of the equilibration as a function of time during the experiment for a measure of one important quantity, the global average precipitation change across the feasible range in entrainment. Specifically, the precipitation change for the highest value of entrainment minus that for the lowest value of entrainment, $\Delta P_{diff}(t) = \Delta P(\mu_{max})-\Delta P(\mu_{min})$, is evaluated as a function of time t, where the precipitation change under global warming ΔP is evaluated for an average centered t years after the start of the end-of-century run minus the corresponding average t years after the start of the historical run. The values μ_{max} and μ_{min} denote the highest and lowest values of the parameter μ, in this case entrainment. This spatial pattern as a function of time is projected onto the 30-year average $\Delta P_{diff\_avg30years}$ which is very similar to the pattern shown in Fig. 2b. In other words, the measure shown is $\langle \Delta P_{diff}(t) \cdot \varphi \rangle$ With $\varphi = \Delta P_{diff\_avg30years} / rms(\Delta P_{diff\_avg30years})$ where angle brackets denote spatial averaging over the globe. The 20-year averages corresponding to the evaluation period used in the main text are shown as horizontal bars. The first 2-year average is close to this value, in other words, a large fraction of the hydrological cycle response is almost equilibrated within the first two years. Subsequent four-year averages essentially complete the equilibration, aside from some internal variability, within the first 10 years. The thickness of the 20-year average bars indicates ±1 standard error for a 20-year average, while the vertical error bars on four-year and two-year averages indicates ±1 standard error for these respective averaging periods.

Error bars for figures 1 and 3 in the main text.

Error bars in Fig. 1 of the main text indicate ±1 standard error in the estimated values, i.e. the repeatability of this measure, estimated from the standard deviation of internal variability for each run. This is estimated by breaking each run into four-year segments to reduce possible effects of interannual correlation. The standard deviation across the set of four-year segments, normalized by $m^{1/2}$, where m is the number of 4-year segments, is computed for the quantity of interest, $rms(P_{exp}-P_{obs})$, where *rms* denotes the spatial root-mean-square, P_{exp} is the precipitation simulated for particular experiment and P_{obs} is observed precipitation from Global Precipitation Climatology Project. The results for different parameter value settings were similar and thus are averaged to yield a single value of the error bar used for each parameter value in Fig. 1.

For Fig. 3 of the main text, the error bars shown are computed using estimates of internal variability based on the ensemble of 15 runs at control parameter values. The projection measure $\langle \Delta P(\mu)\ \Delta P_{\mathrm{diff}} \rangle / \mathrm{rms}(\Delta P_{\mathrm{diff}})$, is calculated for each of the 15 runs, and twice the standard deviation of this is used as the error bar for each of the experiments that has a single run. For the control case, the mean of the 15 runs is displayed with error bars corresponding to a standard error of $n^{-1/2}$ times the standard deviation, where n=15 is the number of runs. An alternate computation of the error bar was also carried out by a method similar to that used in Fig. 1, i.e. the standard deviation of $\langle \Delta P(\mu)\ \Delta P_{\mathrm{diff}} \rangle / \mathrm{rms}(\Delta P_{\mathrm{diff}})$, of the set of 4-year segments normalized by $m^{1/2}$, where *m* is the number of four-year averages, averaging over all experiments. This yielded error bars very similar to the ones displayed.

December-February precipitation sensitivities.

Figure S2 is the same as Fig. 2, but for December-February, showing spatial patterns of precipitation change and precipitation change sensitivity across the feasible range for entrainment, convective timescale, downdraft fraction and evaporation efficiency.

Typical precipitation change patterns for CMIP5 models.

Figure S3 shows precipitation patterns corresponding to Fig. 2a of the main text, but for a selection of models from the CMIP5 archives. The selection is based on models with multiple ensemble members starting from different initial conditions for historical and RCP8.5 simulations. Multi-run ensemble means are formed over the ensemble for each model. Regional differences among these figures may be seen to be of similar order of magnitude as those investigated in the parameter perturbation runs in the main text.

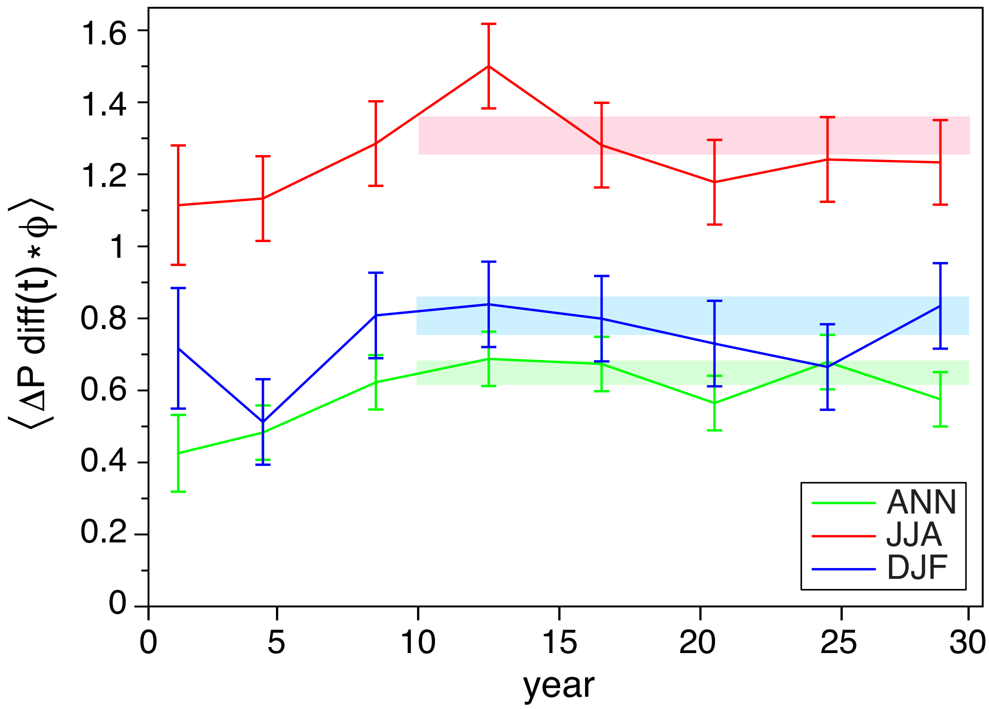

Figure S1. Global average precipitation change across the feasible range of the entrainment parameter (0 to 2×10^{-3} m^{-1}), ΔP_{diff}, by a measure that uses a spatial projection of ΔP_{diff} onto the pattern in Fig. 2b, showing the development of this pattern as a function of time for annual (green), June-August (red) and December-February (blue). The first point is an average over the first two years, subsequent points are four-year averages. Horizontal shaded areas show this measure of precipitation change averaged over the last 20 years, once the signal is approximately equilibrated, with the vertical extent of the shaded area indicating ± 1 standard error about the 20 year mean, as estimated from internal variability as described in the SI text.

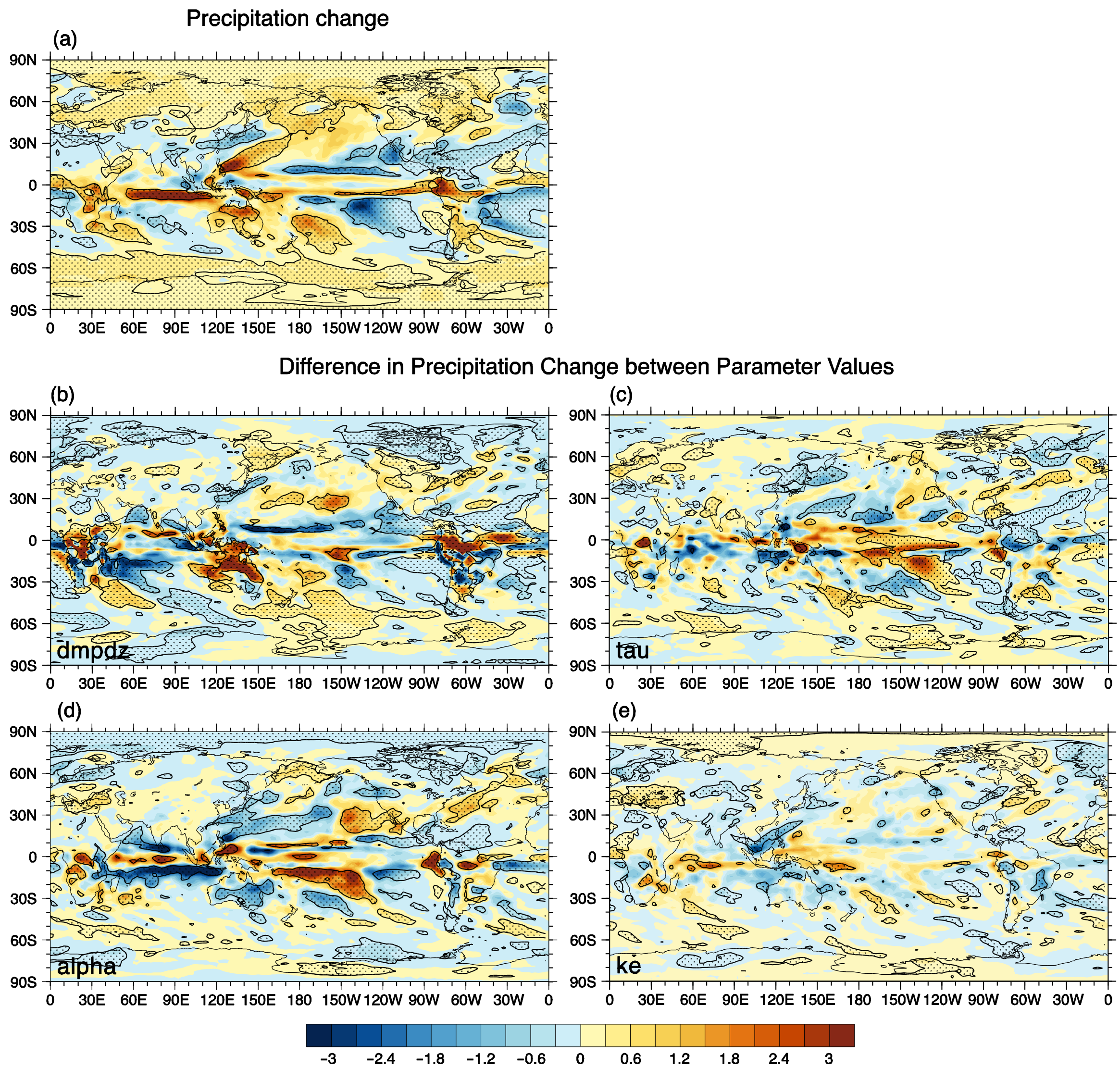

Figure S2. (a) Precipitation (mm/day) change for 2081-2100 relative to the 1986-2005 base period under the RCP8.5 global warming scenario for CESM1 standard values for DJF. (b)-(d) *Differences* in projected DJF precipitation change (mm/day) under global warming (2081-2100 relative to the 1986-2005 base period) for simulations done with different parameter values, corresponding to the JJA case shown in Fig. 2 of the main text. Differences are across the feasible range for each parameter: (b) entrainment (case at 2 x 10^{-3} m^{-1} minus case at 0 m^{-1}); (c) deep convective adjustment time (240 min case minus 30 min case); (d) downdraft fraction (0.75 case minus case at 0); (e) evaporation efficiency (1x10^{-6} (kg m^{-2} s^{-1})$^{-1/2}$ s^{-1} case minus 0.1x10^{-6} (kg m^{-2} s^{-1})$^{-1/2}$ s^{-1} case). Stippled areas pass a t-test at the 95% level.

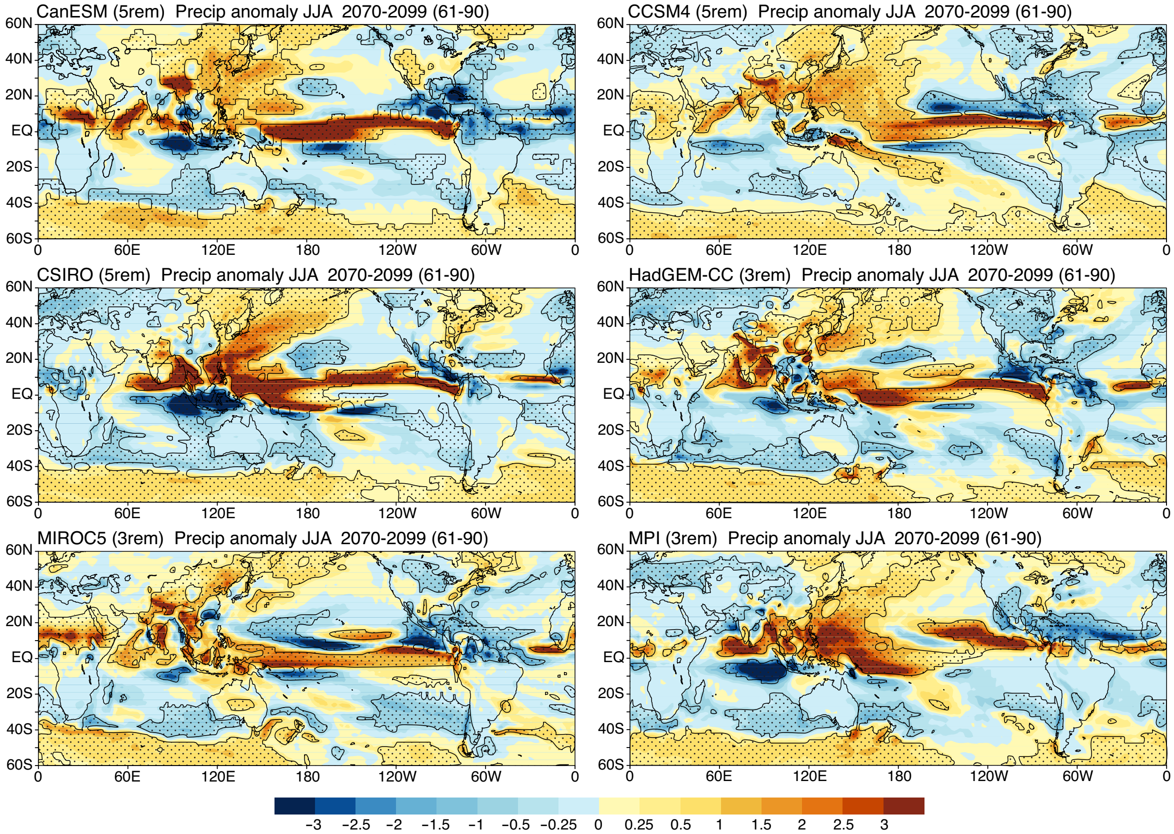

Figure S3. Examples for CMIP5 models Precipitation projections under RCP8.5 scenario for June-Aug. 2070-2099 minus historical base period 1961-1990 for: (a) CanESM (5 members), (b) CCSM4 (5 members), (c) CSIRO (5 members), (d) HadGEM-CC (3 members), (e) MIROC5 (3 members), (d) MPI (3 members). Stippled areas pass a t-test at the 95% level. The number of ensemble members included in the multi-run ensemble mean is indicated in brackets for each model.